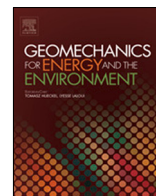




Contents lists available at ScienceDirect

Geomechanics for Energy and the Environment

journal homepage: www.elsevier.com/locate/gete

Cement with bacterial nanocellulose cured at reservoir temperature: Mechanical performance in the context of CO₂ geological storage

Juan Cruz Barría^{a,e}, Diego Manzanal^{b,*}, Patricia Cerrutti^{c,d}, Jean-Michel Pereira^e

^a Facultad de Ingeniería, Universidad Nacional de la Patagonia San Juan Bosco, 9004 Comodoro Rivadavia, Chubut, Argentina

^b E.T.S.I. Caminos, Universidad Politécnica de Madrid, Prof. Aranguren 3, 28040 Madrid, Spain

^c Instituto de Tecnología en Polímeros y Nanotecnología (ITPN), Grupo de Biotecnología y Materiales Biobasados, Universidad de Buenos Aires (UBA), CONICET, Facultad de Ingeniería, Las Heras 2214 (1127), Buenos Aires, Argentina

^d Universidad de Buenos Aires, Facultad de Ingeniería, Departamento de Ingeniería Química, Av. Intendente Güiraldes 2620 (1428) – Pabellón de Industrias, Ciudad Universitaria, Buenos Aires, Argentina

^e Navier, Ecole des Ponts, Univ Gustave Eiffel, CNRS, Marne-la-Vallée, France

ARTICLE INFO

Article history:

Received 2 June 2020

Received in revised form 30 January 2021

Accepted 12 July 2021

Available online xxxx

Editors-in-Chief:

Professor Lyesse Laloui and Professor Tomasz Hueckel

Keywords:

CO₂ geological storage

Cement paste

Bacterial nanocellulose

Reservoir temperature

Chemo-hydro-mechanical couplings

ABSTRACT

Storing CO₂ in deep underground reservoirs is key to reducing emissions to the atmosphere and standing against climate change. However, the risk of CO₂ leakage from geological reservoirs to other rock formations requires a careful long-term analysis of the system. Mostly, oil well cement used for the operation must withstand the carbonation process that changes its poromechanical behavior over time, possibly affecting the system's integrity.

This work focuses on the microstructure and mechanical behavior of cement modified with bacterial nanocellulose (BNC) cured at 90 °C, simulating temperature at the reservoir level. The chemo-hydro-mechanical (CHM) coupled behavior of the cement–rock interface is also investigated through numerical analyses.

Mercury intrusion porosimetry (MIP), X-ray diffraction (XRD), ultrasonic wave velocity measurement, and unconfined compressive strength (UCS) tests were performed on cement samples subjected to a supercritical CO₂ environment. After carbonation, BNC samples show a lower mass gain and lower porosity compared to PC. Permeability based on MIP results indicate that the BNC reduces the permeability of the specimen. XRD quantification shows no substantial difference between the crystalline phases of the two samples. Samples with BNC have lower absolute strength but higher relative increase during carbonation.

The numerical study includes a homogenization of the medium considering the contribution of all components. CHM behavior of the cement with BNC is analyzed, and the results show the variations of the physical and chemical properties across the sample. The numerical study shows the advantage of using this type of tool to study realistic CO₂ injection scenarios in deep wells.

© 2021 The Authors. Published by Elsevier Ltd. This is an open access article under the CC BY-NC-ND license (<http://creativecommons.org/licenses/by-nc-nd/4.0/>).

1. Introduction

There is an increasing rate of greenhouse gas emissions into the atmosphere. This can have consequences for different ecosystems and human health.¹ The carbon dioxide capture and storage (CCS) technology is an effective solution to reduce these emissions of CO₂.² This technology allows storing massive amounts of CO₂ underground in geological reservoirs.^{3,4} It is important to know the storage capacity of the reservoir, but this highly

depends on temperature and pressure. To store CO₂ in a supercritical state (scCO₂), deep reservoirs present considerably higher capacities than shallower reservoirs with similar pore volumes.

Furthermore, high pressures and temperatures just above the supercritical point considerably increase the fluid density, and therefore the amount of CO₂ that can be stored.² Other key factors are the porosity and permeability of the reservoir rock. For instance, the “Sicily Channel” and “Abruzzi Offshore” reservoirs are candidates for geological storage, with porosities reaching 25.6% and permeability of 358 mD.⁵ On the other hand, shale formations can also be considered for storage of CO₂, as indicated by studies on the SACROC Unit reservoir, since shale rock have porosities of around 10% and permeability of 10–100 mD, ensuring that their sealing capacity can be maintained for decades.⁶

* Corresponding author at: E.T.S.I. Caminos, Universidad Politécnica de Madrid, Prof. Aranguren 3, 28040 Madrid, Spain.

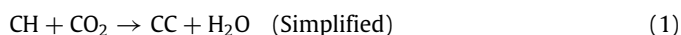
E-mail address: d.manzanal@upm.es (D. Manzanal).

<https://doi.org/10.1016/j.gete.2021.100267>

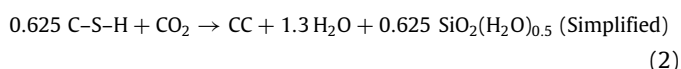
2352–3808/© 2021 The Authors. Published by Elsevier Ltd. This is an open access article under the CC BY-NC-ND license (<http://creativecommons.org/licenses/by-nc-nd/4.0/>).

The caprock formation is an impermeable barrier that covers the upper part of the reservoir and prevents CO₂ leakage to other geological formations. However, during drilling, the zone near the well is damaged. Existing or drilling-induced faults/fractures in the caprock could turn into leakage paths of CO₂ to upper environments. An annular cement barrier is placed between the steel casing and the rock formation to maintain the wellbore integrity after the drilling fluids are removed.

Several problems arise in this system during CO₂ injection, as temperature gradients⁷ and induced seismic activity.⁸ These effects change the stress states and can lead to failure of the cement or rock. Furthermore, Class G cement used in the oil industry is chemically unstable against CO₂ and scCO₂.⁹ Geochemical studies of cement paste show that the advance of carbonic acid through cement paste mainly induces the chemical reaction of portlandite (CH) and hydrated calcium silicates (C–S–H), and the precipitation of calcium carbonate (CC).¹⁰ These chemical reactions induce changes in porosity and the mineral composition of the solid phase. The first reaction of carbonation in cement is between CH and CO₂:



In the absence of CH, the pH level is significantly reduced, allowing the second reaction that consists of the carbonation of the C–S–H:



The formation of amorphous silica from C–S–H could increase porosity, depending on the C–S–H structure,¹¹ and may reduce structural integrity. Furthermore, CaCO₃ precipitated in a water acidified medium in the presence of CO₂ is in turn prone to dissolution.¹² This dissolution continues until thermodynamic equilibrium is reached,¹³ increasing porosity, permeability, and reducing compressive strength.¹⁴ After complete carbonation and degradation, the cement matrix may result in a porous medium of low resistance, unable to maintain the borehole's integrity or the ability to seal against external loads.^{15,16}

The modification of cement to improve some properties is a subject of interest in the cement wellbore industry. The objective is to modify the cement matrix, making it lighter while maintaining high strength and low permeability in its hardened state. New additives such as nanocellulose are being added to the mix to improve the cement properties.¹⁷ Nanocellulose can be used as a crack-inhibitor to avoid cement damage and prevent CO₂ leakage through the upper formations.^{18,19} Bacterial nanocellulose (BNC) is a type of nanocellulose obtained from bacteria of the genus *Gluconacetobacter*. This material is produced by ITPN-UBA-CONICET, and obtained in a more economical and less polluting way than other polymers.²⁰ Nanocellulose is considered a potential additive to improve cement properties, such as mechanical and thermal resistance, and decrease transport phenomena by reducing cement porosity.^{21–24} In turn, its use can be extended in the oil industry in cementing operations.

The effect of bacterial nanocellulose (BNC) on the porosity and mechanical behavior of oil well cement paste cured at 20 °C and atmospheric pressure has been recently studied.^{22,25,26} Barriá et al.²² show that BNC increases compressive strength and thermal stability in non-carbonated samples. BNC-cement samples subjected to scCO₂ conditions show a density increase and a reduction in porosity. The carbonation degree is reduced; therefore, the mechanical behavior is less affected than non-modified cement.²⁵ Nevertheless, its behavior at different curing conditions like those in a reservoir is unknown.

Temperatures in the various geological reservoirs (coal beds, deep saline aquifers, or depleted oil and gas reservoirs) can

vary depending on the depth at which they are found. In some reservoirs, the temperature can vary from 60 to 160 °C²⁷ being 90 °C a value usually used by other authors experimenting with cement.^{28–31}

This work focuses on the microstructure and mechanical changes of cement pastes with added bacterial nanocellulose and cured at 90 °C in the context of CO₂ reservoir conditions. Mercury intrusion porosimetry (MIP), X-ray diffraction (XRD), ultrasonic wave velocity measurement, and unconfined compressive strength (UCS) tests were performed on BNC-cement samples subjected to supercritical CO₂ conditions to characterize its behavior. A finite-element-based numerical analysis of the chemo-hydro-mechanical (CHM) coupled behavior of the cement–rock interface accounting for the obtained experimental data is then carried out to explore realistic scenarios of CO₂ injection in deep wells.

2. Experimental program

Cement samples modified with bacterial nanocellulose were cured at 90 °C, simulating temperature at reservoir level before being carbonated under wet supercritical CO₂ conditions. Porosimetry and mechanical tests were performed on these samples to study the evolution of the microstructure and mechanical behavior.

2.1. Materials

The cement used in this study was Class G Portland Cement. The cement composition obtained by X-ray fluorescence is C₃S 52.8%, C₃A 1.6%, C₂S 21.1% and C₄AF 15.5%.²²

Bacterial nanocellulose (BNC) is a biopolymer derived from the aerobic fermentation of bacteria of the genus *Gluconacetobacter*.³² This biopolymer is a membrane with circa 98% of water and 2% of bacterial nanocellulose. Cerrutti et al.²⁰ shows SEM images of the membrane. Micrometric fibers of nanometric thickness form the membrane. Deionized water and a polycarboxylate ADVA 175 LN High-Performance Water-Reducing Admixture were used in the mixture.

2.2. Preparation of cement samples

Bacterial nanocellulose additive was prepared by grinding the BNC membranes and using ultrasound to generate a homogeneous fluid.²² Cement mixtures were made following the American Petroleum Institute (API) Standard 10 A.³³ The samples in cylindrical molds were cured in a 90 °C batch, unmolded after 24 h, and kept underwater for 48 h. They were then dried at 85 °C for one week,²⁸ simulating a dry cure in the wellbore. A group of 16 samples, 8 non-modified cement (PC) and 8 with 0.05% of BNC (BNC05), were prepared and cored with a diamond wire saw into 76 mm long cylinders with a diameter of 38 mm each.

2.3. Carbonation

The accelerated carbonation under wet supercritical CO₂ conditions was carried out in a vessel of 4020 cm³ of volume at 90 °C and 20 MPa for 30 days. The samples were placed on a container grid inside the cell. 500 ml of water were placed at the bottom of the vessel to maintain humidity. First, the vessel was pressurized with CO₂ until 8 MPa. Then, the temperature of the vessel was raised to 90 °C and the pressure was regulated until 20 MPa. These conditions were maintained during the entire test. Once the test finished, the heating system was turned off, and the pressure was slowly released until atmospheric pressure. Fig. 1 shows the equipment used. 4 Portland Cement (PC) samples and 4 modified

Table 1
MIP tests.

Test	Reference	Curing temperature [°C]	BNC [%]	Carbonation days	Porosity [%]
1	PC-Reference	90	0	0	33.7
2	PC-NC	90	0	0	34.6
3	BNC05-NC	90	0.05	0	34.5
4	PC-30INT	90	0	30	24.5
5	PC-30EXT	90	0	30	21.5
6	BNC05-30INT	90	0.05	30	23.2
7	BNC05-30EXT	90	0.05	30	21.0

cement samples with 0.05% BNC (BNC05) were carbonated for 30 days.

2.4. Porosimetry measurement and permeability estimation

The pore size distributions of the BNC-cement samples were characterized using mercury intrusion porosimetry (MIP). The AutoPore IV 9500 Micromeritics with a maximum pressure of 230 MPa was used to measure pore sizes between 5 nm and 300 μm . Samples of approximately 1 cm^3 were taken from a representative zone of the non-carbonated cement samples. In the carbonated cement case, samples were taken from the core and the most degraded zone near the exposed surface. Before testing, samples were dried by the freeze-drying method.

The effect of curing the samples in the oven (Section 2.2) for 1 week was measured. For this purpose, air-cured samples (PC-Reference) and oven-cured samples (PC-NC and BNC05-NC) were compared. NC means non-carbonated samples, while 30INT and 30EXT are 30 days carbonated samples located at the interior and exterior of the bulk sample, respectively. The tests performed are listed in Table 1.

By assuming cylindrical interconnected pores, we can calculate the pore diameter corresponding to each mercury pressure step by:

$$p = -\frac{4\gamma \cos(\theta)}{d} \quad (3)$$

where γ = mercury surface tension = 0.485 N/m, θ = mercury contact angle = 130° ³⁴, p = mercury pressure, d = pore diameter.

An estimate of permeability can be made from the results obtained in the MIP test. This estimation is performed by considering the macro-scale flow with Darcy's law and the micro-scale flow with Poiseuille's law.

Each pore of class i of diameter d_i has an intrusion volume of mercury V_i , so a length L_i can be determined for each pore class i :

$$L_i = \frac{4V_i}{\pi d_i^2} \quad (4)$$

Assuming laminar flow, the Poiseuille's flow in a cylindrical tube depends on the difference of pressures at the tube ends, the dimensions of the tube, and the viscosity of the fluid. So the flow for each tube of diameter d_i is:

$$Q_{\text{Poiseuille}} = \frac{\Delta V}{\Delta t} = \frac{\Delta P_i (\pi d_i^4)}{128 L_i \eta} \quad (5)$$

Where ΔP_i is every mercury pressure step, and η is the dynamic viscosity of the fluid.

Once the total flow rate is obtained, Darcy's law can determine the permeability at the macro-scale. Let V_t be the total apparent volume of the MIP sample (ratio of total pore volume to porosity). The average pore length L_e is defined as:

$$L_e = \sqrt[3]{V_t} \quad (6)$$

The hydraulic gradient i is given by:

$$i = \frac{\Delta P_t}{L_e} \quad (7)$$

where ΔP_t is the total pressure increase in meters of water column measured in the MIP.

Therefore, the intrinsic permeability of the material (independent of fluid conditions) is:

$$\kappa = \frac{\sum_1^n Q_{\text{Poiseuille}}}{iS} \left(\frac{\eta}{\rho_f g} \right) \quad (8)$$

where n is the total number of pores of different diameters, S is the cross-section of a cubic specimen with sides of length L_e , ρ_f is the density of the fluid, and g is the gravity.

The calculated permeability accounts for an isotropic flux in a cubic sample. Hence, it needs to be divided by three to compare with the directional permeability obtained experimentally. This indicates that the fluid flows equally in the three directions of space.³⁵

The specimens analyzed to calculate permeability were carbonated and non-carbonated samples of both cement types (PC-NC, PC-30EXT, BNC05-NC, BNC05-30EXT).

2.5. X-ray diffraction (XRD)

X-ray diffractograms were obtained in a Philips 3020 diffractometer using $\text{CuK} \alpha$ radiation with a Ni-filter (35 kV, 40 mA). Scanning was performed between 3° and 70° 2θ , with a step of 0.04° and a count time of 2 s/step. The openings of the divergence, reception, and dispersion slots were 1, 0.2, and 1° respectively, and no monochromator was used. The identification of the mineral phases in the material was performed using the X'Pert High Score program. The standard procedures described in the literature and described by Moore and Reynolds³⁶ were followed to identify and quantify the minerals. Quantification was based on the work of Biscaye.³⁷

2.6. Ultrasonic wave measurement

The equipment used was a portable Olympus EPOCH XT detector with P and S ultrasonic waves measurements. Two transducers were placed on the top and bottom surfaces with a thin layer of gel to ensure full contact between the specimen surfaces and the transducers. The time it takes for the P and S elastic wave signals to travel through the sample was measured and divided by the sample's length. The shear and bulk moduli are then calculated by:

$$G = \rho V_s^2 \text{ and } K = \rho \left(V_p^2 - \frac{4}{3} V_s^2 \right) \quad (9)$$

while the Young's Modulus and Poisson coefficient are calculated by:

$$E = \frac{9KG}{3K + G} \text{ and } \nu = \frac{3K - 2G}{6K + 2G} \quad (10)$$

2.7. Mechanical testing

The uniaxial compression tests were performed on a 100 kN universal testing machine by imposing a velocity of 0.5 mm/min. The carbonated and non-carbonated mixtures were tested. The average strength value was calculated from 3 tested cylindrical samples of 38 mm in diameter by 76 mm height. Maximum compression strength and Young's modulus were obtained for all samples.

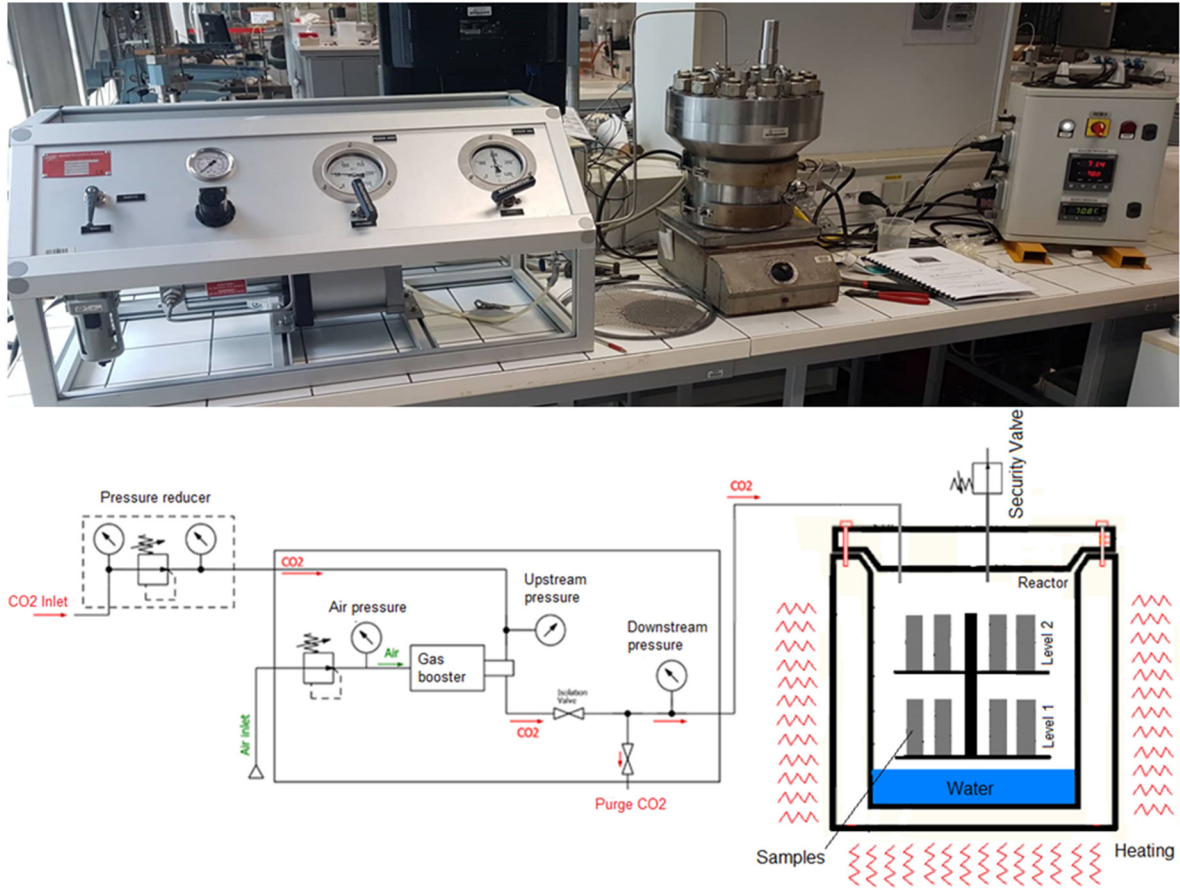


Fig. 1. Carbonation equipment used.

3. Chemo-mechanical analysis of carbonated samples

The experimental study has been complemented by analyzing the chemo-poro-mechanical coupled behavior of the cement with added 0.05% BNC and reacting with the CO_2 . The model simulates the carbonation front advance in cement subjected to scCO_2 and the changes generated by the chemical reactions using the classic balance equations of continuum mechanics relative to mass, momentum, entropy, and energy.^{38,39} It is assumed that the porous solid remains saturated by the fluid (i.e., scCO_2 does not penetrate within the pores of the cement).^{40,41} CO_2 is present in the skeleton as a dissolved species within the fluid.

When cement is carbonated, porosity undergoes several variations. Some are due to chemical reactions, denoted ϕ_L for leaching of cement matrix and ϕ_P for calcite precipitation. The other variations of porosity are due to the deformation of the porous medium, with ϕ_F and ϕ_C as the deformation of the porosity filled by fluid phase and by calcite phase, respectively. The porosities involved can be written as follows:

$$\phi_F = \phi_0 + \phi_L - \phi_P + \phi_F \quad (11)$$

$$\delta_C = \phi_P + \phi_C \quad (12)$$

where ϕ_F corresponds to the pore volume occupied by the in-pore fluid per unit of the initial volume of the porous medium, ϕ_0 corresponds to the initial pore space per unit of the initial porous medium volume, which is not occupied by the solid phase. The difference between these two porosities is denoted by δ_C , which is the pore volume occupied by carbonate crystals.^{38,42}

The constitutive equations of isotropic linear poroelastic material of an infinitesimal representative volume element of a porous

medium ($d\Omega_0$) are derived from Gibbs–Duhem equalities and Clausius–Duhem inequality assuming isothermal conditions:

$$\begin{aligned} \sigma - \sigma_0 &= \left(K - \frac{2}{3} G \right) (\varepsilon - \varepsilon_0) \mathbf{1} + 2G (\varepsilon - \varepsilon_0) \\ &- \sum_{k=F,C} b_k (p_k - p_{k,0}) \mathbf{1} \end{aligned} \quad (13)$$

$$\varphi_J - \varphi_{J,0} = b_J (\varepsilon - \varepsilon_0) + \sum_{k=F,C} \frac{p_k - p_{k,0}}{N_{JK}}; J = F, C \quad (14)$$

where σ and ε are the stress tensor and infinitesimal strain tensor, $\varepsilon = \text{tr}(\varepsilon)$ is the volumetric strain, K and G are the bulk modulus and shear modulus in drained conditions, respectively. φ_J is the deformation of the porous volume occupied by the phase J (F stands for fluid and C for carbonates). Simultaneously, b_J and N_{JK} are the generalized Biot coefficients and the generalized poroelastic coupling moduli.⁴³

The coupling with the chemical reactions taking place during carbonation is established from the mass conservation law of the fluid and CO_2 . Eq. (15) is the fluid mass conservation, while Eq. (16) is the conservation of the molar amount of CO_2 :

$$\begin{aligned} &\left(\rho_f \phi_f + \frac{\rho_f}{N_{FF}} \right) \frac{\partial p_f}{\partial t} + \rho_f b \text{div} \left(\frac{\partial \mathbf{u}}{\partial t} \right) + \rho_f \sum_{R_i} Y_{R_i} \frac{\partial \xi_{R_i}}{\partial t} \\ &- \text{div} \left(\rho_f \frac{\kappa}{\eta} \text{grad } p_f \right) = 0 \\ &\frac{\partial (\phi_f c_{\text{CO}_2})}{\partial t} + \sum_{R_i} a_{R_i} \frac{\partial \xi_{R_i}}{\partial t} \end{aligned} \quad (15)$$

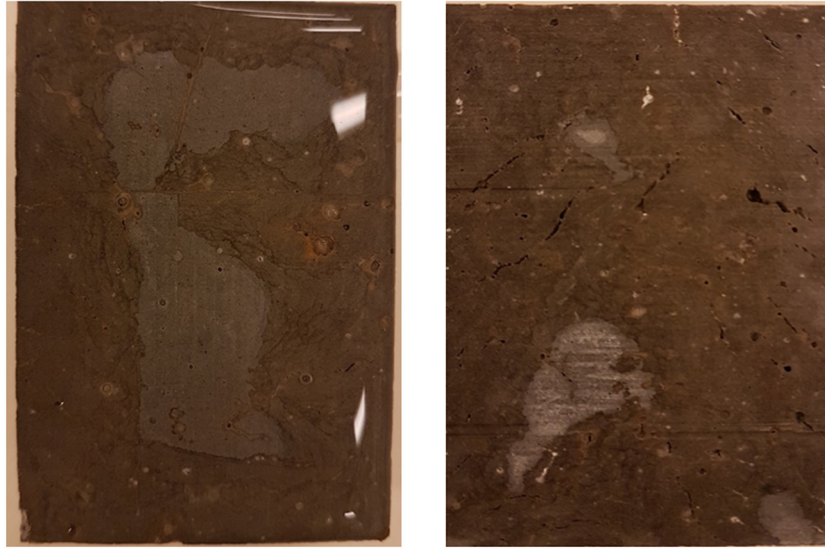


Fig. 2. Samples cured at 90 °C and carbonated for 30 days (left: PC, and right: BNC05).

Table 2
Density and mass uptake after carbonation.

Samples		Initial density [g/cm ³]	Final density [g/cm ³]	Mass gained [%]
1	PC	1.89	2.14	13.5%
2	PC	1.89	2.15	13.5%
3	PC	1.89	2.13	12.4%
4	PC	1.89	2.15	13.4%
5	BNC05	1.87	2.12	13.5%
6	BNC05	1.87	2.13	13.7%
7	BNC05	1.88	2.12	12.6%
8	BNC05	1.87	2.09	11.8%

$$- \operatorname{div} \left(d_{\text{eff}} \mathbf{grad} c_{\text{CO}_2} + c_{\text{CO}_2} \frac{\kappa}{\eta} \mathbf{grad} p_f \right) = 0 \quad (16)$$

where ρ_f , ϕ_f , K_f , p_f are the density, porosity, bulk modulus, and pressure of the fluid. a_{Ri} is the stoichiometric coefficient of the reaction Ri , c_{CO_2} is the CO_2 concentration in fluid, η is the dynamic viscosity of the fluid phase, Y_{Ri} is a variable that depends on the molar volumes of reactive species, \mathbf{u} is the skeleton displacement vector, ξ_{Ri} is the reaction advancement depending on κ and d_{eff} , which are the permeability and diffusion coefficients.

The progress of carbonation is governed by the parameters of CO_2 diffusion in the fluid and by advection:

$$\frac{\partial \xi_{Ri}}{\partial t} = \operatorname{div} \left(d_{\text{eff}} \mathbf{grad} \frac{n_{\text{CO}_2}}{\phi_f} + n_{\text{CO}_2} \frac{\kappa}{\eta} \mathbf{grad} p_f \right) \quad (17)$$

where n_{CO_2} corresponds to the apparent CO_2 concentration. It should be noted that C–S–H carbonation is assumed not to start until the portlandite is completely carbonated since the portlandite maintains a high pH level (pH > 12).

Since the cement is a heterogeneous multiphase material, a homogenization technique was used.⁴⁴ A modification in the homogenization formulation has been introduced to account for the contribution of bacterial nanocellulose (BNC) characteristics to the overall characteristics of modified Portland class G cement. The model is implemented in the finite element code BIL 2.3.0.⁴⁵

Chemical reactions (carbonation-dissolution) occurring in the system induce changes in the transport and mechanical properties of the system. The main parameters that influence the carbonation advance are the intrinsic permeability κ and the diffusion coefficient d_{eff} . Advection behavior is subjected to the

medium permeability and fluid flux, while Fick's Law rules diffusion. Both phenomena are in turn intimately linked to the initial cement porosity.^{46,47} For this type of cement, it can be evaluated using:

$$\kappa = \kappa_0 \left(\frac{\phi_F}{0.26} \right)^{11} 10^{-19} \text{ m}^2 \quad (18)$$

where κ_0 is a parameter to calibrate.

The variation of the porosity in a porous medium must be considered throughout the effective diffusion coefficient. The effective diffusion coefficient is ϕD , while D is the solute diffusion coefficient in the interstitial pore solution. Based on experimental data, Mainguy and Coussy⁴⁸ propose the following expression for the effective coefficient of diffusion:

$$d_{\text{eff}} = d_{\text{eff},0} e^{(9.95\phi_F - 29.08)} \quad (19)$$

being $d_{\text{eff},0}$ a parameter to calibrate.

These equations are empirical and aimed at reasonably representing the transport phenomena occurring within the cement matrix. Parameters κ_0 and $d_{\text{eff},0}$ can be modified to obtain values of intrinsic permeability and diffusivity suitable for class G or H cement.

4. Experimental results and discussion

Fig. 2 shows the longitudinal cut of samples after 30 days of carbonation. Brown color represents the most degraded part of cement due to carbonation, the color probably being due to iron hydroxide released from chemical reactions.⁶ PC samples show a more intact core compared to BNC05.

The penetration depth had significant progress on the cement cured at 90 °C after 30 days of carbonation. These results are similar to observations obtained by other authors for curing and carbonation under similar conditions.^{28,49} There are some uncertainties based on studies by previous authors, mainly from the curing conditions before carbonation. Indeed, water to cement ratio, curing temperature, pressure, and duration will change the carbonation results, so different curing conditions and equal carbonation procedures will yield different results. Some previous experiences have short curing times for the cement,^{28,49} and show high CO_2 penetration, while some other authors considered longer curing periods,^{50,51} showing less penetration. Recent works have shown that cement with lower density allows a

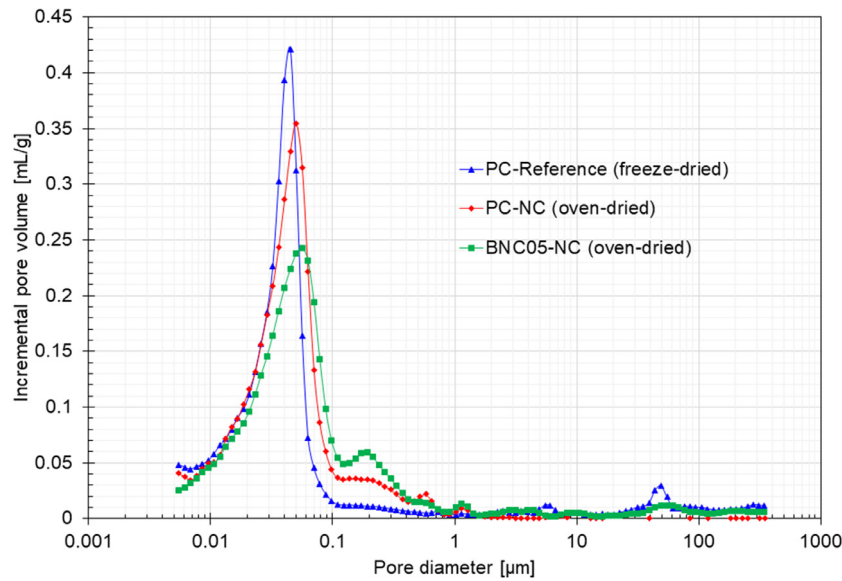


Fig. 3. Pore size distribution variation of oven-dried and non-oven-dried samples.

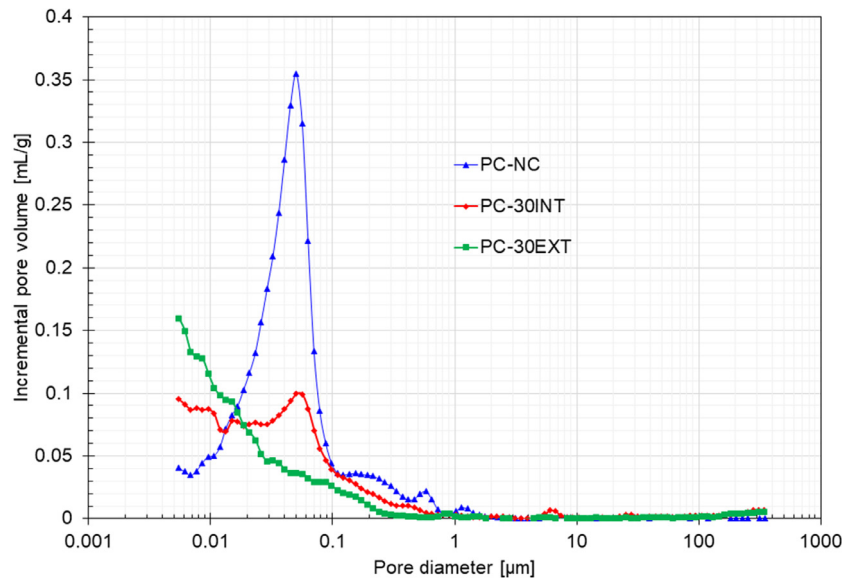


Fig. 4. Pore size distribution of carbonated and non-carbonated PC samples.

Table 3
Intrinsic permeabilities.

Sample	k [m ²]
PC - NC	3.4×10^{-18}
PC - C	3.1×10^{-19}
BNC05 - NC	3.2×10^{-19}
BNC05 - C	2.6×10^{-19}

higher CO₂ penetration.⁵² Furthermore, a higher hydration degree is tied with density increase and porosity reduction⁵³; maintaining a high temperature during a short curing period will allow deeper CO₂ penetration into the cement samples and more advanced chemical reactions.

In this work, carbonation led to an increase in the density of PC and BNC05 samples. Before carbonation, a slight difference is noted between PC and BNC05 samples, with densities of 1.89 and 1.87 g/cm³, respectively. Once the samples were carbonated,

density increased until 2.13 and 2.11 g/cm³ for PC and BNC05 (Table 2). PC shows an average mass uptake of 13.2%, while BNC05 shows an average of 12.9%, meaning that fewer chemical reactions have taken place. The mass gain is similar to previous works under similar conditions⁴⁹; however, the penetration depth is different. Our results are closer to the penetrations observed by Fabbri and co-workers,²⁸ even though our samples are not fully carbonated after 30 days. This is because our samples are larger; therefore, more chemical CO₂-bonds are needed to carbonate more volume, and the diffusion of CO₂ limits chemical reactions.

The oven-drying conditioning for one week at 85 °C has not significantly affected the MIP porosity or the pore size distribution from non-conditioned samples (Fig. 3). MIP porosity performed on these samples increased for both cement types from 33.7% to 34.5%, before the carbonation test, and the characteristic peak is approximately 50 nm. Bacterial nanocellulose did not significantly modify the cement in terms of porosity or pore

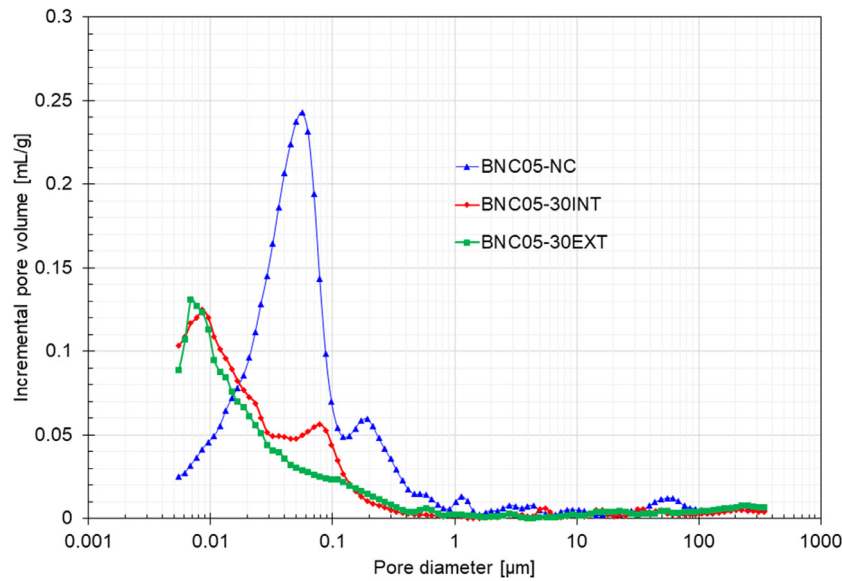


Fig. 5. Pore size distribution of carbonated and non-carbonated BNC05 samples.

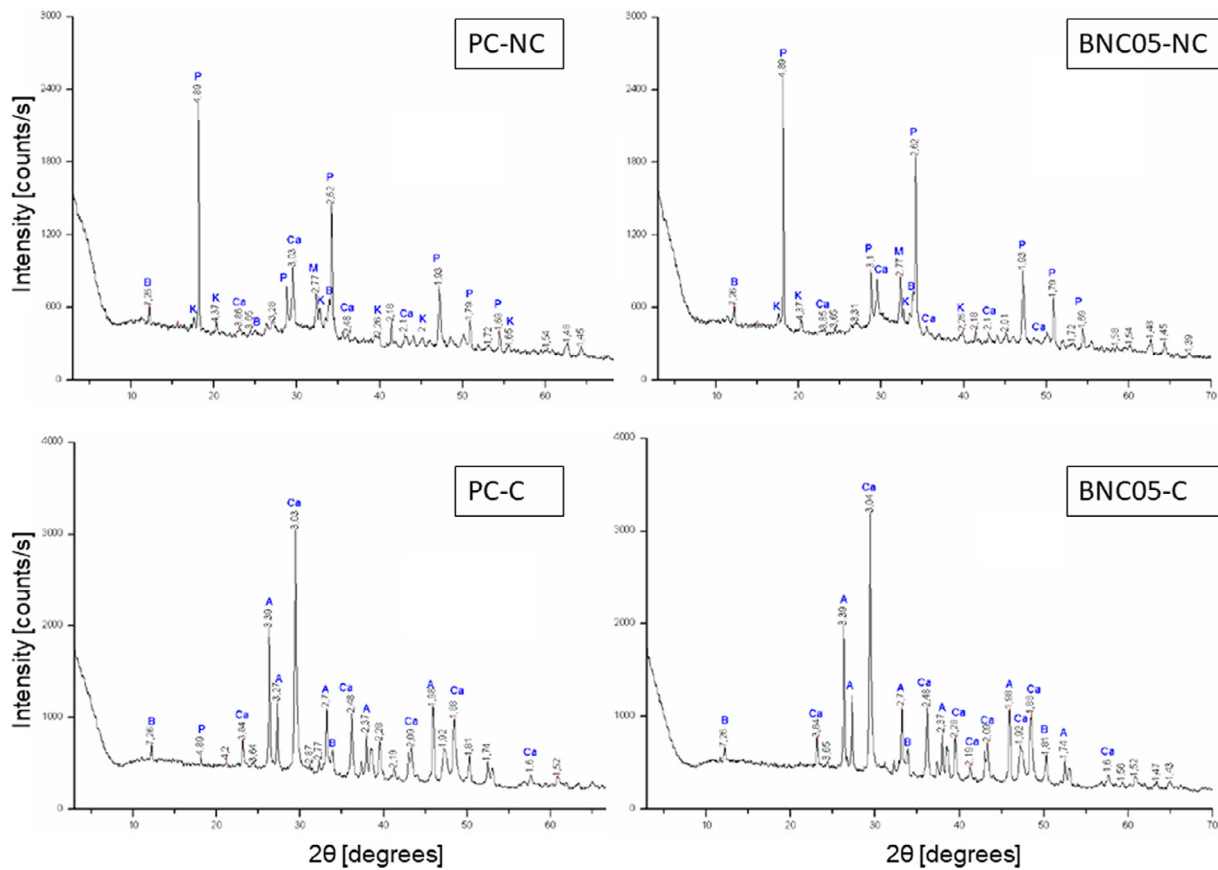


Fig. 6. XRD patterns of non-modified cement (PC) and modified cement (BNC05) before carbonation (NC) and after carbonation (C).

size distribution compared to PC cement cured at 90 °C. Likely, bacterial nanocellulose does not have the same effect in inhibiting the larger cracks produced by the high curing temperature.

Calorimetry tests have shown that BNC initially acts as a cement retarder.^{54,55} As the curing time in this work is short, the porosity of BNC-cement is similar to PC with some coarser pores at 0.2 μm. Nevertheless, for more extended curing periods (p.e. cement cured at 20 °C for 28 days), the cement structure is denser

and more compact. In these conditions, bacterial nanocellulose is more likely to develop a fiber network inside the cement and increment hydration degree,^{56,57} as it tends to release adsorbed water, which contributes to the hydration.¹⁸

The MIP results after the carbonation of PC are presented in Fig. 4. Here we can observe that the porosity variation along the radial direction leads to smaller pores and smaller porosity values. At the same time, the characteristic peak is shifted to pores

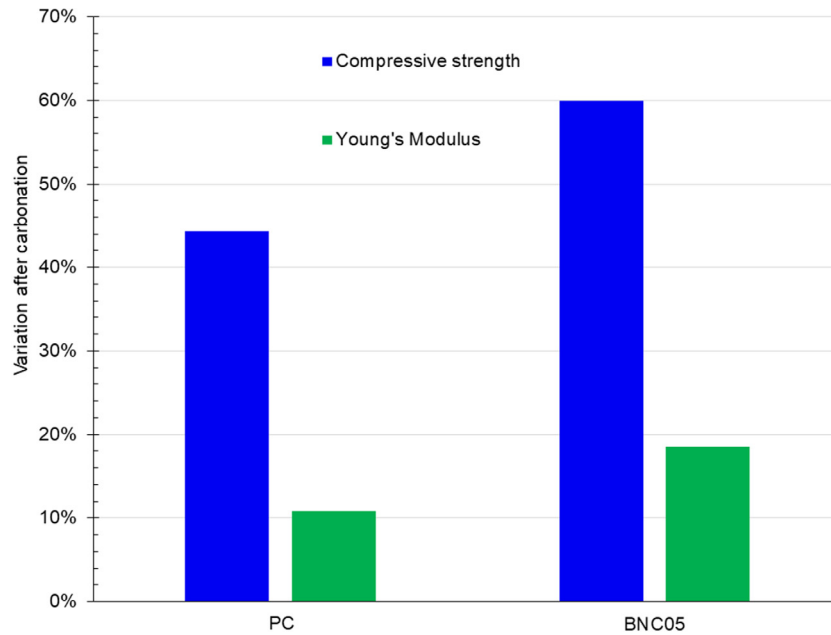


Fig. 7. Compressive strength and Young's Modulus variation after carbonation of PC and BNC05 samples.

smaller than 10 nm. After carbonation, no significant change is observed due to the addition of BNC. Porosity decreased to 24.5% at the core and to 21.5% near the exposed surface. BNC05 shows similar results to PC (Fig. 5), and its porosity decreased at the core to 23.2% and near the exposed surface to 21%. The slight mass uptake is due to the consumption of CO_2 by the occurring chemical reactions and is reflected by these small porosity variations. Reduced porosities lead to less diffusion of CO_2 into the cement core and therefore increase the time to reach full carbonation of the samples.

The permeability results in Table 3 are consistent with the intrinsic permeability values of cement cured at a high temperature. This method simplifies the complexity of crosslinking between different cylinders of different pore diameters and considers a tortuosity of 1.⁵⁸ The lengths (L_i) are very high for small diameter pores, so a higher deviation error is also induced.

In this analysis, cement with nanocellulose addition appears to have lower permeability than cement without additions. After carbonation, the permeability values of PC are reduced by one order of magnitude. In contrast, the permeability in cement with BNC addition is in the same order of magnitude as the initial value. Results on carbonated cement samples require experimental validation.

Fig. 6 presents the XRD patterns of the samples before and after carbonation. The relative percentages of the crystalline phases are presented in Table 4. The analyses show the contents of portlandite, katoite, brownmillerite, magnesite, aragonite, and calcite. Portlandite is one of the main cement hydration products with high crystallinity. In contrast, C-S-H is a low crystallinity amorphous material. Brownmillerite is a phase of clinker denominated as C_4AF . Aragonite and calcite are calcium carbonates of a different crystalline system with orthorhombic and rhombohedral shapes, respectively. When the curing temperature is high, new crystalline phases such as katoite appear. Katoite is a calcium aluminate hydrate more stable at high temperatures than ettringite.

XRD results on cement before supercritical carbonation (Table 4) show approximately 60% hydrated material (portlandite and katoite), 25% carbonated material (calcite and magnesite),

Table 4

Relative percentage of the crystalline phases before and after exposure.

Crystalline phase (%)	PC sample		BNC05 sample	
	NC	C	NC	C
Portlandite	32	1	33	–
Katoite	28	–	29	–
Magnesite	10	–	5	–
Brownmillerite	16	6	15	7
Calcite	14	43	18	44
Aragonite	–	50	–	49

Table 5

Elastic properties measured by elastic waves velocities V_p and V_s .

Sample	G [GPa]	K [GPa]	E [GPa]	ν
PC - NC	8.4	9.5	19.5	0.16
PC - C	8.9	12.7	21.3	0.22
BNC05 - NC	7.8	8.5	18	0.15
BNC05 - C	8.9	9.8	20.5	0.15

and 15% non-hydrated and non-carbonated material (brownmillerite). It can be observed that 25% of crystalline material is already carbonated during the curing process before supercritical carbonation. The lack of crystals related to C-S-H is due to the insufficient intensity of reflection of this amorphous material.⁵⁹ It is possible that the short curing time has generated a low reflection tobermorite and that the small readings have been incorporated into the crystalline phase of the katoite or calcite.

XRD results on cement after supercritical carbonation show no cement hydration materials (portlandite and katoite). Therefore, it signifies complete carbonation. Magnesite also seems to have been consumed, allowing the formation of more calcium carbonates. Approximately 93% are crystalline carbonate materials; the remaining 7% is C_4AF from the clinker phase that did not chemically react.

The results of the PC and BNC05 samples before and after carbonation are similar to each other, suggesting that the BNC did not significantly affect the microcrystalline structure of the cement under these curing conditions.

Table 5 shows the mechanical properties measured by V_s and V_p . Overall, during the carbonation process, mechanical properties

increase. UCS tests corroborate this result. The samples show an increment in compressive strength and their Young's modulus (Fig. 7). PC strength initially was 31 MPa, and after the carbonation stage, it increased by 44%, while BNC05 started with 24 MPa of strength, which increased by 60% with carbonation. Both types of cement initially had Young's modulus of 20 GPa, unlike the 25 GPa in long-cured specimens,²⁵ but after carbonation, this modulus increased by 11% for PC and by 18% for BNC05.

Nanocellulose has been reported to improve the mechanical properties of cement composites for well-hydrated cement.^{19,60,61} In the present work, BNC05 samples initially have less compressive strength than PC samples and comparable Young modulus. These observations distinguish from the results previously obtained with cement cured at room temperature over a long period.²² Curing at a higher temperature is probably generating larger cracks in the cement, so the microstructural effect of BNC does not substantially improve the mechanical behavior. Alternatively, this effect appears later because of the retarder effect of BNC or the superplasticizer, which slow down the hydration rate of the modified cement, and thus the hydration degree at the end of the curing time.

It is well known that carbonation under atmospheric conditions tends to increase the mechanical properties of cement.^{62,63} However, there is no agreement on cement strength variations after supercritical carbonation.⁴⁹ In supercritical conditions, some results show an increment in compressive strength,^{64,65} while more recent researchers were able to see a decrease in mechanical performance.^{28,66,67} This variation is due to different conditions of cement hydration prior to carbonation⁶⁸ and subsequent carbonation conditions.⁶⁵ Indeed, experiments using the same cement and water to cement ratio and same carbonation conditions show a drop in strength values.²⁵ After short curing conditions, cement will not be fully hydrated. Therefore, the mechanical performance increment after carbonation will most likely be due to the cement matrix development by hydration acceleration imposed by temperature in the carbonation cell. The tested material's mechanical properties will be a combination of the effects of cement hydration compounds and precipitated calcite produced during carbonation.

On the other hand, well-hydrated cement will only experience a drop in strength due to C-S-H degradation and porosity increase over time.^{25,51,67,69} In this work, supercritical carbonation is positively affecting the mechanical performance of cement. These observations are intricately linked to the carbonation conditions. Indeed, if cement carbonation is imposed by a continuously renewed fluid, then the products of carbonation (mainly carbonates), will in turn dissolve and be flushed out, leading to a strong increase in porosity of the cement, and degraded mechanical properties. In the present experiment, CO₂ penetrates the sample by dissolution and diffusion in the pore fluid, which is not renewed.

Since CC has better mechanical performance than CH, CC precipitation should increase mechanical performance and Young's modulus of carbonated cement. This effect can occur here because of the continuous hydration of cement inside the reactor, which links the precipitated CC with the cement matrix. These two effects increase mechanical properties, as seen by Fabbri et al. and Sauki et al.,^{28,65} but cement hydration plays the most significant role during the carbonation process. This can also be observed from V_p and V_s wave data, where mechanical parameters increased. However, Young's moduli differ from the ones measured by UCS tests. Young's moduli measured by elastic waves are 19.5 and 21.3 GPa for PC before and after carbonation, while for BNC05, measured values were 18 and 20.5 GPa. UCS tests gave values of 20 GPa for both types of cement samples before

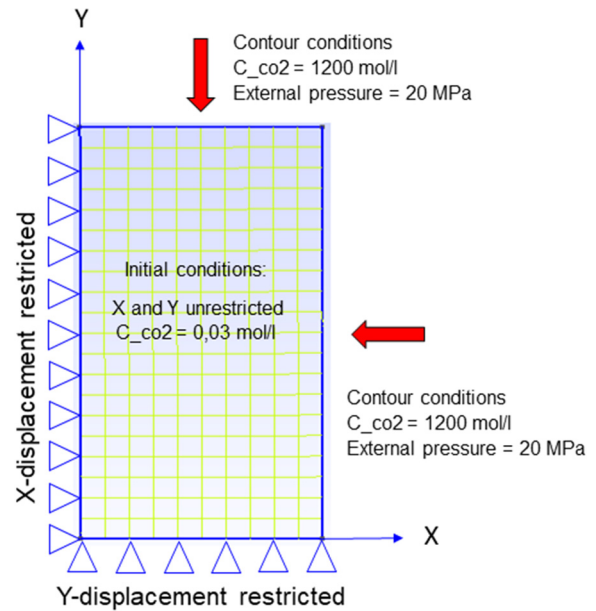


Fig. 8. 2D model. Representation of one-quarter sample subjected to carbonation using the code BIL.

carbonation, while after carbonation, these values were 22.2 GPa and 23.6 GPa for PC and BNC05, respectively.

After carbonation, Fig. 7 shows that the increase in the relative strength and Young modulus of BNC05 is more significant than for PC. BNC samples enhanced the hydration kinetics due to: (1) the hydrophilic properties of the bacterial nanocellulose⁵⁷; and (2) its ability to release water during hydration.¹⁸

5. Numerical analysis of carbonated samples

In this section, the numerical analysis of the carbonated BNC samples is presented. A 2D analysis is performed simulating the experimental carbonation of the cylindrical samples. Calibration on the model is made by taking the porosity values obtained experimentally to estimate the intrinsic parameters of this cement.⁷⁰ The initial volumetric proportions of the minerals in the cement are estimated from the literature. The calibrated model is extrapolated to simulate in 1D the cement carbonation in a wellbore system under downhole conditions.

5.1. Initial parameters and intrinsic properties of cement

Porosity is very variable for cement and depends mainly on the water to cement ratio and on the type of curing in which the specimen is placed. Some authors estimate porosities greater than 30%,^{30,49,71,72} while others approximate it from 20% to 30%.^{73–76} Regardless of the kind of oil cement in question (G or H), it can be generalized that the porosities of oil cement are around 25% to 35%. The initial porosity of the samples in this work before carbonation is 34.5%, as indicated in Section 4.

The volumetric content of cement minerals depends substantially on the cement type, water to cement ratio, hydration degree, and curing temperature. So, it is necessary to estimate these proportions for the simulation. In some articles, the amount of Portlandite CH varies between 15 to 25%,^{46,74} with commonly accepted values being percentages of 18 to 20%.³⁸ In previous results, using the same cement and same water to cement ratio,²² a percentage of 20% was obtained by thermogravimetric analysis on well-hydrated cement samples. Class G and H cement have

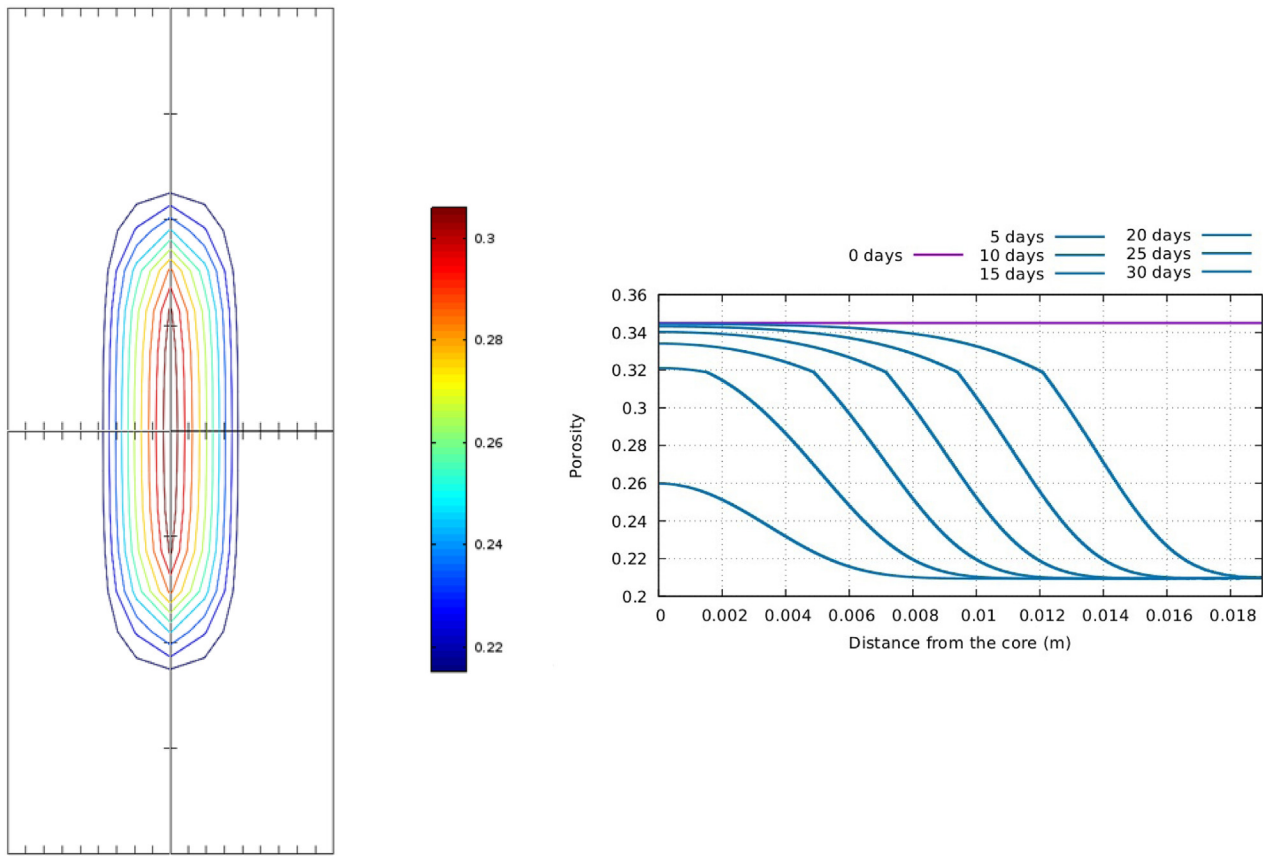


Fig. 9. Left: Results of the simulation showing the variation of porosity in the experimental BNC05 sample of 38 mm by 78 mm for values of $\kappa_0 = 350$ and $d_{eff,0} = 160$. Right: Results of porosity in 1D.

very low initial aluminate contents following API requirements to be resistant to sulfate attacks ($C3A \leq 3\%$ and $C4AF + 2 C3A \leq 24\%$). So the hydrated aluminate components have a low percentage, around 6 to 14%.^{38,73,77} Finally, the essential cement phase in terms of compressive strength, C-S-H, can vary between 60 to 27% in volume fraction.^{38,77}

The intrinsic permeability is independent of the conditions to which the material is initially subjected, at least directly. Since the cement is a heterogeneous material, there is no unique intrinsic permeability value for cement. Nelson et al.⁷⁸, in their experiments, report values of $1 \times 10^{-16} \text{ m}^2$ to $1 \times 10^{-20} \text{ m}^2$. This is supported by Ghabezloo et al.⁷⁴ and Mainguy et al.⁷⁹, who obtain values in the order of $1 \times 10^{-19} \text{ m}^2$ y $1 \times 10^{-20} \text{ m}^2$. Sercombe et al.⁷⁶ show values of $1 \times 10^{-16} \text{ m}^2$ after excessive heating on hardened cement paste, so it can be assumed that this order of magnitude refers to cracked cement.

The diffusivity of cement of class G and H has also been variable, as reported by different authors. Huet et al.⁸⁰ perform a compilation of the different transport mechanisms of cement G subjected to an environment of scCO_2 and quotes diffusivity values of $1 \times 10^{-12} \text{ m}^2\text{s}^{-1}$ down to $1 \times 10^{-14} \text{ m}^2\text{s}^{-1}$. Mainguy et al.⁷⁹ give an example of diffusion in the order of $1 \times 10^{-12} \text{ m}^2\text{s}^{-1}$, and Vallin et al.³⁸ determine a value of $1 \times 10^{-10} \text{ m}^2\text{s}^{-1}$ on the simulation. Furthermore, Shen⁸¹ quotes the values of different aqueous species in the order of $1 \times 10^{-9} \text{ m}^2\text{s}^{-1}$.

To obtain the diffusion and permeability parameters for this particular cement for later use in the simulation at reservoir level, a porosity value equal to the experimental value of 34.5% for the first simulation is considered. As the rest of the volumetric proportions are variable, values were adopted from literature

Table 6
Initial media properties for simulations.

η_{vis} [MPa.s]	K_F [MPa]	ρ_F [kg/m ³]	R_c [MPa]	R_t [MPa]
$0.5 \cdot 10^{-9}$	2200	1000	24	2.4

Table 7
Molar volumes in cm³/mol.

v_{CH}^S	$v_{C-S-H_{1.6}}^S$	$v_{CaCO_3}^S$	$v_{SiO_2(H_2O)_{0.5}}^S$	$v_{H_2O}^F$
33.1	84.7	36.9	31	18.85

Table 8
Initial properties for the downhole simulation.

Inclusion	Volumetric prop. PC-BNC	Bulk modulus [GPa]	Shear modulus [GPa]
Porosity	0.345	–	–
CH	0.18	33.00	14.50
C-S-H	0.405	25.00	18.40
Aluminates	0.06942	27.00	9.50
Calcite	0.00	69.00	37.40
BNC	0.00058	42.00	38.00

considering a 0.05% content of BNC: C-S-H 40.5%, CH 18%, aluminates 6.942%, and BNC 0.058%. The remaining compounds are classified as inert components, including amorphous silica, which is a carbonation product. CO_2 concentration is calculated considering: water volume, temperature, pressures, and mole fraction of CO_2 from experiments. The calculations give values of 1200 mol/m³.

Table 9Values of κ for different values of κ_0 .

Porosity	Parameter κ_0 [m ²]					
	0.1	1	10	100	350	500
0.345	2.24E-19	2.24E-18	2.24E-17	2.24E-16	7.86E-16	1.12E-15

Table 10Values of d_{eff} for different values of $d_{eff,0}$.

Porosity	Parameter $d_{eff,0}$ [m ² /s]					
	0.1	1	10	100	160	300
0.345	7.27E-13	7.27E-12	7.27E-11	7.27E-10	1.16E-9	2.18E-9

The initial parameters for fluid and cement are listed in Table 6, where η_{vis} is the fluid viscosity, K_F the fluid compressibility, ρ_F is the fluid density, R_c is cement compressive strength, and R_t the tensile strength. Table 7 shows the molar volumes of the compounds involved.

The 2D model for the experimental carbonation consists of one-quarter of a sample (19 mm-radius by 38 mm-height) using a mesh of 22×11 elements (Fig. 8). The lower horizontal contour has restricted movements in the X direction, while the left vertical contour has restricted movements in the Y direction. The top and right-hand contours are subjected to the carbonation conditions. Table 8 shows the initial conditions for modeling.

The well-system modeled consists of a CO₂ reservoir drilled and refilled with a steel casing protected by a cement annulus. We used the same transport values after determining the advection and diffusion parameters from the previous simulation. The model for the wellbore simulation assumes 1D axial symmetry under plane strain conditions in the axial direction. The mesh of $\frac{3}{4}$ of an inch (19 mm) represents the annular cement thickness and allows studying the carbonation progress from the outer surface towards the inner cement. It consists of 502 elements that have the properties of the modified cement with BNC. Previous conditions for temperature and fluid pressure are considered (that is 90 °C and 20 MPa) with a 1.2 CO₂ molarity.

5.2. Results and discussion

First, a sensitivity analysis of parameters to calibrate the numerical model is made to reproduce the experimental penetration results. Tables 9 and 10 show the values of the intrinsic permeability and diffusion coefficient varying κ_0 and $d_{eff,0}$. As it can be observed, the values of permeability and diffusivity are in the range of the admissible values for cement class G previously mentioned.

By calibrating the model for $\kappa_0 = 350$ and $d_{eff,0} = 160$, a representation of the entire sample consistent with the MIP experimental results of porosity can be observed in Fig. 9. Results clearly show how the carbonation advanced into the core. The 1D image shows the porosity variation as a function of the radius. The material near the exposed surface is completely carbonated, and the porosity reaches 21%, while at the core, the porosity average is similar to the 23.2% from the MIP experiments.

Fig. 10 shows in more detail the dissolution and carbonation fronts. The blue line corresponds to the starting point of the chemical reaction of CH. In contrast, the red line is the limit between the carbonation process and the full carbonated zone. Some authors consider that the carbonation front or penetration depth follows a linear trend as a function of the square root of time (consistently because the chemical reactions are limited by the diffusion of CO₂ within the fluid phase).^{82,83} Nevertheless, this is usually based on the phenolphthalein test, which only considers the pH below 9. With the present model, we can distinguish

the two fronts. In a first contact between the cement and scCO₂, there is a significant decrease in CH and C-S-H content that lasts for the first few days. After 10 days, the dissolution front reaches the center of the cement sample. The complete reaction of CH and C-S-H front advances almost linearly in time but, it does not reach the cement center. Calcite is mostly deposited in the material near the exposed surface, decreasing its porosity, while it has not yet wholly precipitated in the core.

Even though the dissolution front has reached the center, the chemical reactions between CO₂ and CH/C-S-H, which produce CC and water, are still taking place in a region located 1 cm away from the center. This means that all CH and C-S-H leaching is not complete after 30 days in these conditions.

The calibrated parameters are extrapolated to the cement submitted under downhole conditions in the context of CO₂ geological storage. We have to keep in mind that curing and carbonation conditions are unfavorable to cement in the experimental results. However, the numerical model can be adapted to any condition considered. From this approach, additional characteristics of the carbonation front variability using these transport parameters can be obtained: permeability (Fig. 11) and volumetric proportions (Fig. 12) variations throughout the sample. Carbonation advance forms calcite from CH and C-S-H, which grows inside the pores. This produces a reduction of the porosity and, consequently, a decrease in permeability and diffusivity, which slow down the entry of more CO₂ to the cement core. In Fig. 11, this can be seen as a clogging effect. After 5 days of carbonation, we can observe a considerable CO₂ penetration, but after 5 more days, the penetration rate has significantly slowed down. The calcite penetration in Fig. 12 starts with the CH area dissolution and continues with the C-S-H decalcification when there is no longer CH to consume. C-S-H decalcification continues creating CC and amorphous silica, which becomes part of the inert components.

6. Conclusion

The microstructure and mechanical changes of cement with bacterial nanocellulose additions and cured at 90 °C in the context of reservoir conditions were analyzed. Mercury intrusion porosimetry (MIP), X-ray diffraction (XRD), ultrasonic wave measurements, and unconfined compressive strength (UCS) tests were performed on BNC-cement samples subjected to supercritical CO₂ conditions to determine its behavior. In addition, a finite-element based numerical analysis of the cement-rock interface was presented.

BNC samples show a lower mass gain compared to PC, suggesting that fewer chemical reactions occurred. Nevertheless, the BNC-cement longitudinal sections present some small voids in their interior, which could allow further CO₂ penetration.

The MIP results show that initially, the BNC samples have the same porosity as the cement without BNC addition. After carbonation, lower porosity is observed in cement with BNC, either in the core or near the exposed surface. From the MIP curves, a permeability analysis was performed. In this analysis, the samples with BNC show lower intrinsic permeability values than the cement without BNC.

The XRD results of the PC and BNC05 samples before and after carbonation show no difference from each other. After carbonation, the dominant crystalline phases are calcite and aragonite, which indicates the complete carbonation of the material near the surface exposed to the gas.

Unmodified samples show a better mechanical performance during carbonation. However, carbonation in samples with BNC indicates a higher increase in relative strength than in samples without additions due to the BNC effect of releasing water during hydration inside the carbonation cell.

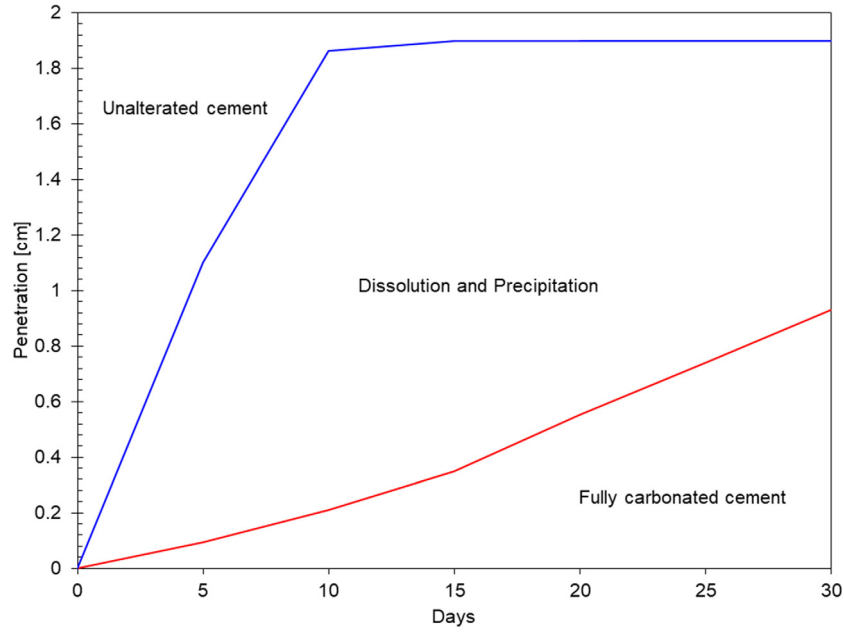


Fig. 10. Dissolution and carbonation fronts development over time.

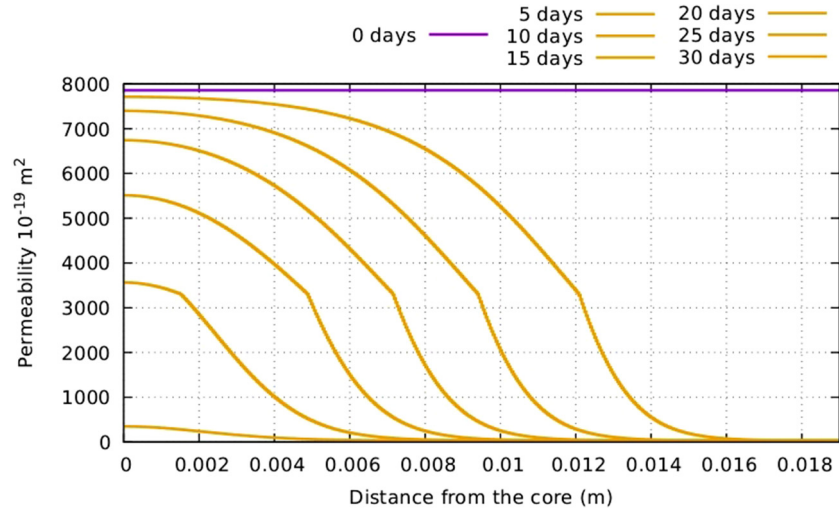


Fig. 11. Permeability variation over time along the annular cement thickness of $\frac{3}{4}$ inch.

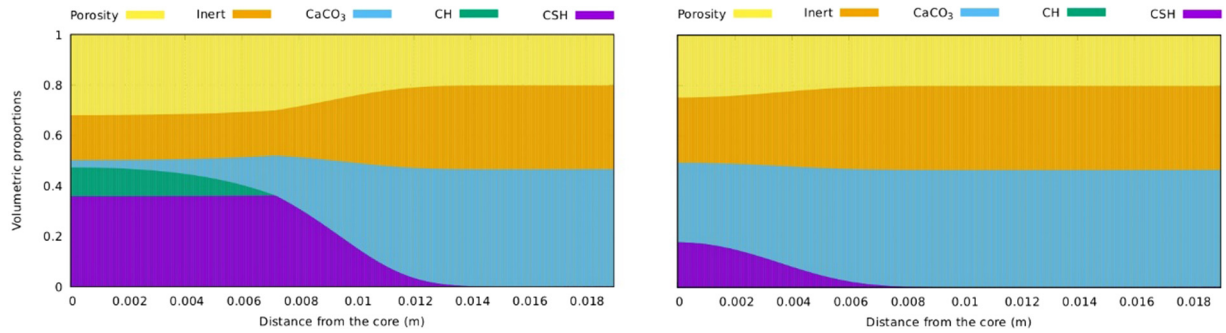


Fig. 12. Volumetric proportions after 15 and 30 days of carbonation along the annular cement thickness of $\frac{3}{4}$ inch.

A chemo-poro-mechanical model of scCO_2 attack on a cement annulus of an abandoned oil well in the context of CO_2 storage was presented. A modification on the formulation was

implemented to add the nanocellulose characteristics. The experimental data and simulation results were back analyzed to

determine the properties of the cement used. Once these properties were known, a simulation under downhole conditions in the context of CO₂ geological storage was represented.

Results show a decrease in permeability and hydration products over time and the advance of the dissolution and carbonation fronts. The numerical study shows the advantage of using this type of tool to study possible real scenarios of CO₂ injection processes in deep wells. It can be adapted to different systems under different established conditions.

Nomenclature

γ : Mercury surface tension

δ_C : Pore volume occupied by carbonate crystals

ΔP_i : Mercury pressure step

ΔP_t : Total pressure increment in meters of water column measured in the MIP

ϵ : Infinitesimal strain tensor

ϵ : Volumetric strain. ($\text{tr}(\epsilon)$)

η : Dynamic viscosity of the fluid phase

θ : Mercury contact angle

κ : Intrinsic permeability

ν : Poisson's ratio

ξ_{Ri} : Reaction advance

ρ : Bulk density of the specimen

ρ_f : Fluid density

σ : Stress tensor

ϕ_C : Deformation of the porous medium filled by calcite phase

ϕ_F : Deformation of the porous medium filled by fluid phase

ϕ_J : Deformation of the porous volume occupied by the phase J

ϕ_0 : Pore space per unit of the initial volume of the porous medium not occupied by the solid phase

ϕ_f : Fluid porosity

ϕ_F : Pore volume occupied by the in-pore fluid per unit volume of the porous medium

ϕ_L : Porosity due to leaching of the cement matrix

ϕ_P : Porosity due to calcite precipitation

a_{Ri} : Stoichiometric coefficient of the reaction Ri

b_j : Generalized Biot coefficient

c_{CO_2} : Is the CO₂ concentration in the fluid

d_i : Pore diameter

d_{eff} : Diffusion coefficient

i : Hydraulic gradient

L_i : Cylinder length of diameter i

L_e : Average pore length

n : Total number of pores of different diameters

n_{CO_2} : Apparent CO₂ concentration

p : Mercury pressure

p_f : Fluid pressure

u : Skeleton displacement vector

E : Young's Modulus

G : Shear Modulus

K : Bulk modulus

K_f : Fluid bulk modulus

N_{JK} : Generalized poroelastic coupling moduli

S : cross-section of a cubic specimen with sides of length L_e

V_i : Volume of mercury intrusion into the pore of diameter i

V_s : Elastic S-wave velocity

V_t : Total apparent volume of the MIP sample

V_P : Elastic P-wave velocity

Y_{Ri} : Variable that depends on the molar volumes of reactive species

CRedit authorship contribution statement

Juan Cruz Barría: Investigation, Validation, Formal analysis, Data curation, Visualization, Writing - original draft. **Diego Manzanal:** Conceptualization, Methodology, Resources, Writing - review & editing, Supervision, Project administration, Funding acquisition. **Patricia Cerrutti:** BNC supplier, Funding acquisition. **Jean-Michel Pereira:** Conceptualization, Methodology, Resources, Writing - review & editing, Supervision, Funding acquisition.

Declaration of competing interest

The authors declare that they have no known competing financial interests or personal relationships that could have appeared to influence the work reported in this paper.

Acknowledgments

The first author gratefully acknowledges the fellowship granted by the National Scientific and Technical Research Council of Argentina (CONICET) and the EIFFEL fellowship program of Excellence granted by the Ministère de l'Europe et des Affaires étrangères of France. The authors acknowledge the European Commission's financial support -H2020 MSCA-RISE 2020 Project DISCO2-STORE, Grant Agreement N° 101007851, the Universidad Nacional de la Patagonia San Juan Bosco, Argentina -Project UNPSJB PI1614 80020190200006 IP, Res. R/9N°207-2020 CRD1365 FI004/ 17-, the Agency of Scientific and Technological Promotion from the Argentine Republic. (Projects PICT 2016-4543, PICT 0843 2016), and the Institutional project ITPN PUE 0034 (CONICET), Argentina. The authors also thank Dr. Siavash Ghabezloo and Dr. Teresa Piqué for helpful discussions and the technical staff of Petroquímica Comodoro Rivadavia and Laboratoire Navier for helping with the tests performed.

Funding

(1) Consejo Nacional de Investigaciones Científicas y Técnicas (CONICET) (2) the Agency of Scientific and Technological Promotion (Agencia Nacional de Promoción Científica y Tecnológica) from Ministry of Science, Technology and Innovation of the Argentine Republic (3) the EIFFEL fellowship program of Excellence granted by the Ministère de l'Europe et des Affaires étrangères of France (4) European Commission (H2020 MSCA.RISE).

Intellectual property

We confirm that we have given due consideration to the protection of intellectual property associated with this work and that there are no impediments to publication, including the timing of publication, with respect to intellectual property. In so doing we confirm that we have followed the regulations of our institutions concerning intellectual property.

References

- Afroz R, Hassan MN, Ibrahim NA. Review of air pollution and health impacts in Malaysia. *Environ Res*. 2003;92(2):71–77. [http://dx.doi.org/10.1016/S0013-9351\(02\)00059-2](http://dx.doi.org/10.1016/S0013-9351(02)00059-2).
- Ringrose Philip. *How to Store CO₂ Underground: Insights from Early-Mover CCS Projects*. Springer; 2020.
- Michael K, Golab A, Shulakova V, et al. Geological storage of CO₂ in saline aquifers – A review of the experience from existing storage operations. *Int J Greenh Gas Control*. 2010;4(4):659–667. <http://dx.doi.org/10.1016/j.ijggc.2009.12.011>.
- Bachu S, Bonijoly D, Bradshaw J, et al. CO₂ storage capacity estimation: Methodology and gaps. *Int J Greenh Gas Control*. 2007;1(4):430–443. [http://dx.doi.org/10.1016/S1750-5836\(07\)00086-2](http://dx.doi.org/10.1016/S1750-5836(07)00086-2).
- Civile D, Zecchin M, Forlin E, et al. CO₂ geological storage in the Italian carbonate successions. *Int J Greenh Gas Control*. 2013;19:101–116. <http://dx.doi.org/10.1016/j.ijggc.2013.08.010>.
- Carey JW, Wig M, Chipera SJ, et al. Analysis and performance of oil well cement with 30 years of CO₂ exposure from the SACROC Unit, West Texas, USA. *Int J Greenh Gas Control*. 2007;1(1):75–85. [http://dx.doi.org/10.1016/S1750-5836\(06\)00004-1](http://dx.doi.org/10.1016/S1750-5836(06)00004-1).
- Vilarrasa V, Laloui L. Potential fracture propagation into the caprock induced by cold CO₂ injection in normal faulting stress regimes. *Geomech Energy Environ*. 2015;2:22–31. <http://dx.doi.org/10.1016/j.gete.2015.05.001>.
- Urpi L, Rinaldi A, Rutqvist J, Cappa F, Spiers CJ. Dynamic simulation of CO₂-injection-induced fault rupture with slip-rate dependent friction coefficient. *Geomech Energy Environ*. 2016;7:47–65. <http://dx.doi.org/10.1016/j.gete.2016.04.003>.
- Mason HE, Du Frane WL, Walsh SDC, Dai Z, Charnvanichborikarn S, Carroll SA. Chemical and mechanical properties of wellbore cement altered by CO₂ - rich brine using a multianalytical approach. *Environ Sci Technol*. 2013;47:1745–1752. <http://dx.doi.org/10.1021/es3039906>.
- Fernández Bertos M, Simons SJR, Hills CD, Carey PJ. A review of accelerated carbonation technology in the treatment of cement-based materials and sequestration of CO₂. *J Hazard Mater*. 2004;112(3):193–205. <http://dx.doi.org/10.1016/j.jhazmat.2004.04.019>.
- Shah V, Scrivener K, Bhattacharjee B, Bishnoi S. Changes in microstructure characteristics of cement paste on carbonation. *Cem Concr Res*. 2018;109(April):184–197. <http://dx.doi.org/10.1016/j.cemconres.2018.04.016>.
- Matteo EN, Huet B, Jové-Colón CF, Scherer GW. Experimental and modeling study of calcium carbonate precipitation and its effects on the degradation of oil well cement during carbonated brine exposure. *Cem Concr Res*. 2018;113(May 2017):1–12. <http://dx.doi.org/10.1016/j.cemconres.2018.03.016>.
- Kim S, Santamarina JC. Reactive fluid flow in CO₂ storage reservoirs: A 2-D pore network. *Greenh Gases Sci Technol*. 2015;473(5):462–473. <http://dx.doi.org/10.1002/ghg>.
- Lesti M, Tiemeyer C, Plank J. CO₂ stability of Portland cement based well cementing systems for use on carbon capture & storage (CCS) wells. *Cem Concr Res*. 2013;45(1):45–54. <http://dx.doi.org/10.1016/j.cemconres.2012.12.001>.
- Abid K, Gholami R, Choate P, Nagaratnam BH. A review on cement degradation under CO₂-rich environment of sequestration projects. *J Nat Gas Sci Eng*. 2015;27:1149–1157. <http://dx.doi.org/10.1016/j.jngse.2015.09.061>.
- Teodoriu C, Bello O. A review of cement testing apparatus and methods under CO₂ environment and their impact on well integrity prediction – Where do we stand? *J Pet Sci Eng*. 2020;187:106736. <http://dx.doi.org/10.1016/j.petrol.2019.106736>.
- Sun X, Wu Q, Lee S, Qing Y, Wu Y. Cellulose nanofibers as a modifier for rheology, curing and mechanical performance of oil well cement. *Sci Rep*. 2016;6:1–9. <http://dx.doi.org/10.1038/srep31654>.
- Hisseine OA, Omran AF, Tagnit-Hamou A. Influence of cellulose filaments on cement paste and concrete. *J Mater Civ Eng*. 2018;30(6):1–14. [http://dx.doi.org/10.1061/\(ASCE\)MT.1943-5533.0002287](http://dx.doi.org/10.1061/(ASCE)MT.1943-5533.0002287).
- Hisseine OA, Wilson W, Sorelli L, Tolnai B, Tagnit-Hamou A. Nanocellulose for improved concrete performance: A macro-to-micro investigation for disclosing the effects of cellulose filaments on strength of cement systems. *Constr Build Mater*. 2019;206:84–96. <http://dx.doi.org/10.1016/j.conbuildmat.2019.02.042>.
- Casaburi A, Cerrutti P, Vázquez A, Foresti ML. Carboxymethyl cellulose with tailored degree of substitution obtained from bacterial cellulose. 2018;75:147–156. <http://dx.doi.org/10.1016/j.foodhyd.2017.09.002>.
- Mejdoub R, Hammi H, Suñol JJ, Khitouni M, Boufi S. Nanofibrillated cellulose as nanoreinforcement in Portland cement: Thermal, mechanical and microstructural properties. *J Compos Mater*. 2017;51(17):2491–2503. <http://dx.doi.org/10.1177/0021998316672090>.
- Barriá JC, Vázquez A, Pereira JM, Manzanal D. Effect of bacterial nanocellulose on the fresh and hardened states of oil well cement. *J Pet Sci Eng*. 2021;199. <http://dx.doi.org/10.1016/j.petrol.2020.108259>.
- Hoyos CG, Zuluaga R, Gañán P, Pique TM, Vazquez A. Cellulose nanofibrils extracted from fique fibers as bio-based cement additive. *J Clean Prod*. 2019;235:1540–1548. <http://dx.doi.org/10.1016/j.jclepro.2019.06.292>.
- Barriá JC, Manzanal DG, Martín CM, Piqué T, Pereira JM. Cement-rock interface subjected to SCCO₂. In: *Rock Mechanics for Natural Resources and Infrastructure Development- Proceedings of the 14th International Congress on Rock Mechanics and Rock Engineering*. 2020:3196–3203.
- Barriá JC, Manzanal D, Ghabezloo S, Pereira J-M. Effect of supercritical carbonation on porous structure and mechanical strength of cementitious materials modified with bacterial nanocellulose. *Cem Concr Compo*. 2021. Submitted for publication.
- Barriá JC, Manzanal D, Pereira JM, Ghabezloo S. CO₂ geological storage: Microstructure and mechanical behavior of cement modified with a biopolymer after carbonation. In: *E3S Web Conf*. 2020:205. <http://dx.doi.org/10.1051/e3sconf/202020502007>.
- Liu X, Falcone G, Alimonti C. A systematic study of harnessing low-temperature geothermal energy from oil and gas reservoirs. *Energy*. 2018;142:346–355. <http://dx.doi.org/10.1016/j.energy.2017.10.058>.
- Fabbri A, Corvisier J, Schubnel A, et al. Effect of carbonation on the hydro-mechanical properties of Portland cements. *Cem Concr Res*. 2009;39(12):1156–1163. <http://dx.doi.org/10.1016/j.cemconres.2009.07.028>.
- Yurtas I, Xie SY, Burlion N, Shao JF, Saint-Marc J, Garnier A. Influence of chemical degradation on mechanical behavior of a petroleum cement paste. *Cem Concr Res*. 2011;41(4):412–421. <http://dx.doi.org/10.1016/j.cemconres.2011.01.008>.
- Rimmelé G, Barlet-gouédard V, Porcherie O, Goffé B, Brunet F. Heterogeneous porosity distribution in Portland cement exposed to CO₂ - rich fluids. *Cem Concr Res*. 2008;38:1038–1048. <http://dx.doi.org/10.1016/j.cemconres.2008.03.022>.
- Samudio M. Modelling of an oil well cement paste from early age to hardened state: hydration kinetics and poromechanical behaviour To cite this version. 2018.
- Charreau HL, Foresti M, Vazquez A. Nanocellulose patents trends: A comprehensive review on patents on cellulose nanocrystals, microfibrillated and bacterial cellulose. *Recent Pat Nanotechnol*. 2012;7(1):56–80. <http://dx.doi.org/10.2174/18722105130106>.
- API specification 10A. In: *Specification for Cements and Materials for Well Cementing*. Twenty-Fif. Northwest Washington, DC: 2019. https://www.techstreet.com/standards/api-spec-10a?product_id=2038411.
- Zeng Q, Li K, Fen-Chong T, Dangla P. Analysis of pore structure, contact angle and pore entrapment of blended cement pastes from mercury porosimetry data. *Cem Concr Compos*. 2012;34(9):1053–1060. <http://dx.doi.org/10.1016/j.cemconcomp.2012.06.005>.
- Khaddour F, Grégoire D, Pijaudier-Cabot G. A hierarchical model for the computation of permeation properties of porous materials and their enhancement due to microcracks. *J Eng Mech*. 2018;144(2):04017160. [http://dx.doi.org/10.1061/\(asce\)em.1943-7889.0001392](http://dx.doi.org/10.1061/(asce)em.1943-7889.0001392).
- Moore D, Reynolds R. X-ray diffraction and the identification and analysis of clay minerals. 1989.
- Biscaye PE. Geological society of america bulletin mineralogy and sedimentation of recent deep-sea clay in the atlantic ocean and adjacent seas and oceans. *Geol Soc Am Bull*. 1965;76(7):803–832. [http://dx.doi.org/10.1130/0016-7606\(1965\)76](http://dx.doi.org/10.1130/0016-7606(1965)76).

38. Vallin V, Pereira JM, Fabbri A, Wong H. Numerical modelling of the hydro-chemo-mechanical behaviour of geomaterials in the context of CO₂ injection. (April):2013:3052–3069. <http://dx.doi.org/10.1002/nag>.
39. Vallin V. Modélisation chimio poromécanique du comportement des géomatériaux dans le contexte du stockage géologique du dioxyde de carbone: Application au puits d'injection. 2014.
40. Manzanal D, Vallin V, Pereira JM. A chemo-poromechanical model for well/caprock interface in presence of CO₂. In: *Poromechanics V - Proc 5th Biot Conf Poromechanics*. 2013:1470–1477. <http://dx.doi.org/10.1061/9780784412992.175>.
41. Fabbri A, Jacquemet N, Seyedi DM. A chemo-poromechanical model of oilwell cement carbonation under CO₂ geological storage conditions. *Cem Concr Res*. 2012;42(1):8–19. <http://dx.doi.org/10.1016/j.cemconres.2011.07.002>.
42. Manzanal D, Pereira JM. Effects of the presence of CO₂ at the well/caprock interface: Crystallization damage. In: *Proceedings of the International Conference on Offshore Mechanics and Arctic Engineering - OMAE*. Vol 6. 2013:1–7. <http://dx.doi.org/10.1115/OMAE2013-11543>.
43. Coussy O. Mechanics and physics of porous solids. 2010. <http://dx.doi.org/10.1002/9780470710388>.
44. Ulm FJ, Constantinides G, Heukamp FH. Is concrete a poromechanics material? - A multiscale investigation of poroelastic properties. *Mater Struct Constr*. 2004;37(265):43–58. <http://dx.doi.org/10.1617/14100>.
45. Dangla P, Bonnard A. Ifsttar/bil: first version in github (Version v2.4). Zenodo. 2017. <http://dx.doi.org/10.5281/zenodo.1039729>.
46. Mainguy M. Modeles de diffusion non-lineaires en milieux poreux. Applications a la dissolution et au séchage des matériaux cimentaires. 1999.
47. Ghabezloo S. Comportement thermo-poro-mécanique d'un ciment pétrolier. 2008:204.
48. Mainguy M, Coussy O. Propagation fronts during calcium leaching and chloride penetration. *J Eng Mech*. 2000;126(3):250–257. [http://dx.doi.org/10.1061/\(asce\)0733-9399\(2000\)126:3\(250\)](http://dx.doi.org/10.1061/(asce)0733-9399(2000)126:3(250)).
49. Barlet-Gouedard V, Rimmelé G, Goffé B, Porcherie O. Well technologies for CO₂ geological storage: CO₂-resistant cement. *SPE Int*. 2007;62(3):325–334. <http://dx.doi.org/10.2516/ogst>.
50. Kutchko BG, Strazisar BR, Dzombak DA, Lowry GV, Thaulow N. Degradation of well cement by CO₂ under geologic sequestration conditions. *Environ Sci Technol*. 2007;41(13):4787–4792. <http://dx.doi.org/10.1021/es062828c>.
51. Gu T, Guo X, Li Z, et al. Coupled effect of CO₂ attack and tensile stress on well cement under CO₂ storage conditions. *Constr Build Mater*. 2017;130:92–102. <http://dx.doi.org/10.1016/j.conbuildmat.2016.10.117>.
52. Costa BL de S, Freitas JC de O, Melo DM de A, Araujo RG de S, d Oliveira YH, Simão CA. Evaluation of density influence on resistance to carbonation process in oil well cement slurries. *Constr Build Mater*. 2019;197:331–338. <http://dx.doi.org/10.1016/j.conbuildmat.2018.11.232>.
53. Bahafid S. A multi-technique investigation of the effect of hydration temperature on the microstructure and mechanical properties of cement paste. 2017. <https://pastel.archives-ouvertes.fr/tel-01980576>.
54. Fu T, Montes F, Suraneni P, Youngblood J, Weiss J. The influence of cellulose nanocrystals on the hydration and flexural strength of Portland cement pastes. *Polymers (Basel)*. 2017;9(9). <http://dx.doi.org/10.3390/polym9090424>.
55. Cao Y, Tian N, Bahr D, et al. The influence of cellulose nanocrystals on the microstructure of cement paste. *Cem Concr Compos*. 2016;74:164–173. <http://dx.doi.org/10.1016/j.cemconcomp.2016.09.008>.
56. Lee HJ, Kim SK, Lee HS, Kim W. A study on the drying shrinkage and mechanical properties of fiber reinforced cement composites using cellulose nanocrystals. *Int J Concr Struct Mater*. 2019;13(1). <http://dx.doi.org/10.1186/s40069-019-0351-2>.
57. Cao Y, Zavaterri P, Youngblood J, Moon R, Weiss J. The influence of cellulose nanocrystal additions on the performance of cement paste. *Cem Concr Compos*. 2015;56:73–83. <http://dx.doi.org/10.1016/j.cemconcomp.2014.11.008>.
58. Ecay L, Grégoire D, Pijaudier-Cabot G. On the prediction of permeability and relative permeability from pore size distributions. *Cem Concr Res*. 2020;133(March):106074. <http://dx.doi.org/10.1016/j.cemconres.2020.106074>.
59. Melzer R, Eberhard E. Phase identification during early and middle hydration of tricalciumsilicate (Ca₃SiO₅). *Cem Concr Res*. 1989;19(c):411–422.
60. Sun X, Wu Q, Zhang J, Qing Y, Wu Y, Lee S. Rheology, curing temperature and mechanical performance of oil well cement: Combined effect of cellulose nanofibers and graphene nano-platelets. *Mater Des*. 2017;114:92–101. <http://dx.doi.org/10.1016/j.matdes.2016.10.050>.
61. Akhlaghi MA, Bagherpour R, Kalhori H. Application of bacterial nanocellulose fibers as reinforcement in cement composites. *Constr Build Mater*. 2020;241:118061. <http://dx.doi.org/10.1016/j.conbuildmat.2020.118061>.
62. Jeong J, Sardini P, Ramézani H, Siitari-Kauppi M, Steeb H. Modeling of the induced chemo-mechanical stress through porous cement mortar subjected to CO₂: Enhanced micro-dilatation theory and 14C-PMMA method. *Comput Mater Sci*. 2013;69:466–480. <http://dx.doi.org/10.1016/j.commatsci.2012.11.031>.
63. Jang JG, Lee HK. Microstructural densification and CO₂ uptake promoted by the carbonation curing of belite-rich Portland cement. *Cem Concr Res*. 2016;82:50–57. <http://dx.doi.org/10.1016/j.cemconres.2016.01.001>.
64. Bruckdorfer RA. Carbon dioxide corrosion in oilwell cements. *Soc Pet Eng*. 1986. <http://dx.doi.org/10.2118/15176-MS>.
65. Sauki A, Irawan S. Effects of pressure and temperature on well cement degradation by supercritical CO₂. *Int J Eng Technol*. 2010;10(4):53–61.
66. Lesti M, Tiemeyer C, Plank J. CO₂ stability of Portland cement based well cementing systems for use on carbon capture & storage (CCS) wells. *Cem Concr Res*. 2013;45(1):45–54. <http://dx.doi.org/10.1016/j.cemconres.2012.12.001>.
67. Xu B, Yuan B, Wang Y, Zeng S, Yang Y. Nanosilica-latex reduction carbonation-induced degradation in cement of CO₂ geological storage wells. *J Nat Gas Sci Eng*. 2019;65(February):237–247. <http://dx.doi.org/10.1016/j.jngse.2019.03.013>.
68. Costa BL de S, Freitas JC de O, Santos PHS, Melo DM de A, Araujo RG da S, de Oliveira YH. Carbonation in oil well Portland cement: Influence of hydration time prior to contact with CO₂. *Constr Build Mater*. 2018;159:252–260. <http://dx.doi.org/10.1016/j.conbuildmat.2017.10.103>.
69. Morandeau A, Thiéry M, Dangla P. Impact of accelerated carbonation on OPC cement paste blended with fly ash. *Cem Concr Res*. 2015;67:226–236. <http://dx.doi.org/10.1016/j.cemconres.2014.10.003>.
70. Barriá JC, Manzanal D, Pereira JM. CO₂ geological storage: Performance of cement-rock interface. In: *Proceedings of the XVI Pan-American Conference on Soil Mechanics and Geotechnical Engineering*. Cancún: 2019:2873–2881. <http://dx.doi.org/10.3233/STAL190359>.
71. Ershadi V, Ebadi E, Rabani AR, Ershadi L, Soltanian H. Reduction of set cement permeability in oil well to decrease the pollution of receptive environment using spherical nanosilica. In: *2nd International Conference on Environmental Science and Technology*. Vol 6. 2011:101–104.
72. Krakowiak KJ, Thomas JJ, Musso S, James S, Akono A, Ulm F. Cement and concrete research nano-chemo-mechanical signature of conventional oil-well cement systems: Effects of elevated temperature and curing time. *Cem Concr Res*. 2015;67:103–121. <http://dx.doi.org/10.1016/j.cemconres.2014.08.008>.
73. Neves A, Romildo J, Toledo D, Jo F. A study of CO₂ capture by high initial strength Portland cement pastes at early curing stages by new non-conventional thermogravimetry and non-conventional differential thermal analysis. *J Therm Anal Calorim*. 2017. <http://dx.doi.org/10.1007/s10973-017-6326-0>.
74. Ghabezloo S, Sulem J, Saint-Marc J. Evaluation of a permeability-porosity relationship in a low-permeability creeping material using a single transient test. *Int J Rock Mech Min Sci*. 2009;46(4):761–768. <http://dx.doi.org/10.1016/j.ijrmm.2008.10.003>.
75. Bahafid S, Ghabezloo S, Duc M, Faure P, Sulem J. Effect of the hydration temperature on the microstructure of Class G cement: C–S–H composition and density. *Cem Concr Res*. 2017;95:270–281. <http://dx.doi.org/10.1016/j.cemconres.2017.02.008>.
76. Sercombe J, Galle C. Rehydration and microstructure of cement paste after heating at temperatures up to 300 °C. 33, 2003:1047–1056. [http://dx.doi.org/10.1016/S0008-8846\(03\)00005-X](http://dx.doi.org/10.1016/S0008-8846(03)00005-X).
77. Ghabezloo S. Cement and Concrete Research Effect of the variations of clinker composition on the poroelastic properties of hardened class G cement paste. *Cem Concr Res*. 2011;41(8):920–922. <http://dx.doi.org/10.1016/j.cemconres.2011.03.022>.
78. Nelson Erik B, et al. *Well Cementing*. Schlumberger Educational Services. 1990.
79. Mainguy M, Mod MM. Mod ' eles de diffusion non linéaire en milieux poreux. Applications a la dissolution et au séchage des matériaux cimentaires. 1999.
80. Huet B, Tasoti V, Khalfallah I. Energy Procedia A review of Portland cement carbonation mechanisms in CO₂ rich environment. *Energy Procedia*. 2011;4:5275–5282. <http://dx.doi.org/10.1016/j.egypro.2011.02.507>.
81. Shen J. Reactive transport modeling of CO₂ through cementitious materials under CO₂ geological storage conditions. 2013.
82. Kutchko BG, Strazisar BR, Lowry GV, Dzombak Da, Thaulow N. Rate of CO₂ attack on hydrated class H well cement under geologic sequestration conditions. *Environ Sci Technol*. 2008;42(16):6237–6242. <http://dx.doi.org/10.1021/es800049r>.
83. Morandeau A, Thiéry M, Dangla P. Investigation of the carbonation mechanism of CH and C–S–H in terms of kinetics, microstructure changes and moisture properties. *Cem Concr Res*. 2014;56:153–170. <http://dx.doi.org/10.1016/j.cemconres.2013.11.015>.